

# Velocity measurements in the near field of a diesel fuel injector by ultrafast imagery

David Sedarsky · Saïd Idlahcen · Claude Rozé · Jean-Bernard Blaisot

Received: 22 July 2012/Revised: 27 November 2012/Accepted: 21 December 2012

**Abstract** This paper examines the velocity profile of fuel issuing from a high pressure single-orifice diesel injector. Velocities of liquid structures were determined from time-resolved ultrafast shadow images, formed by an amplified two-pulse laser source coupled to a double-frame camera. A statistical analysis of the data over many injection events was undertaken to map velocities related to spray formation near the nozzle outlet as a function of time after start of injection (SOI). These results reveal a strong asymmetry in the liquid profile of the test injector, with distinct fast and slow regions on opposite sides of the orifice. Differences of  $\sim 100$  m/s can be observed between the ‘fast’ and ‘slow’ sides of the jet, resulting in different atomization conditions across the spray. On average, droplets are dispersed at a greater distance from the nozzle on the ‘fast’ side of the flow, and distinct macrostructure can be observed under the asymmetric velocity conditions. The changes in structural velocity and atomization behavior resemble flow structures which are often observed in the presence of string cavitation produced under controlled conditions in scaled, transparent test nozzles. These observations suggest that widely-used common-rail supply configurations and modern injectors can potentially generate asymmetric interior flows which strongly influence diesel spray morphology. The velocimetry measurements presented in this work represent an effective and relatively straightforward approach to identify deviant flow behavior in real diesel sprays, providing new spatially resolved information on fluid structure and flow characteristics within the shear-layers on the jet periphery.

**Keywords** diesel sprays · velocity · cavitation · image correlation velocimetry

## 1 Introduction

At present, there are a number of well-known physical phenomena in spray flows which are not fully understood, in the sense that their complete behavior cannot be predicted. High pressure injection used to atomize liquid fuel in combustion applications is a prime example. The full atomization process results in a droplet granularity which cannot be fully controlled by injection parameters, e.g. injection pressure, nozzle geometry, etc. (Shavit and Chigier, 1995). In the case of diesel fuel injection, interactions between different parameters on a variety of scales complicate a full description of the injection process. These difficulties include: small orifice diameters ( $\sim 100$   $\mu\text{m}$ ), high injection pressures ( $\sim 200$  MPa), large optical depths, and short injection durations. Recent work in direct numerical simulation (DNS) applied to liquid injection phenomena has demonstrated that realistic simulations of spray events are possible (Ménard et al., 2007; Lebas et al., 2009), albeit at the cost of large computation times. However, the validation of numerical models with experimental results remains a challenge. Good quality visualizations of diesel fuel sprays may be found in the literature, though spray regions with large optical depth ( $OD$ ) are typically under-resolved or inaccessible. Recently, a number of innovative visualization techniques have been developed to address the difficulties presented by multiple scattering in sprays, e.g. ballistic imaging (Sedarsky et al., 2006, 2009, 2011; Linne et al., 2009; Idlahcen et al., 2012), X-ray diagnostics (Ramírez et al., 2009), and background reduction schemes (Kristensson et al., 2010).

While time-resolved images can capture important information related to the atomization process, the character-

D. Sedarsky · S. Idlahcen · C. Rozé · J-B. Blaisot  
UMR 6614 CORIA, CNRS, Université et INSA de Rouen  
BP 12, avenue de l'Université  
76801 Saint Etienne du Rouvray Cedex, France  
Tel.: +33(0)23-295-3691  
Fax: +33(0)23-291-0485  
E-mail: david.sedarsky@coria.fr

ization of the spray must include the spatially-resolved instantaneous velocity to fully describe the injection features. Measurements of near-nozzle spray regions which include such information can be used to track the kinematics of spray formation, revealing the inception and growth of small instabilities which grow to dominate the downstream spray behavior and drive the atomization process. In turn, this information can serve to validate numerical simulations of primary breakup and spray morphology.

The near-nozzle regions of practical sprays are often easily disturbed, precluding the use of diagnostics which perturb the flow conditions. Measurements of liquid velocities in diesel sprays are further complicated by the small relative scale of the spray features compared to the magnitude of the flow velocity (on the order of  $\sim 500$  m/s). Although a number of optical techniques are routinely applied to track fluid motion at this scale and magnitude, most are unsuitable for application in the vicinity of a dense stream of fuel. This is due in large part to the numerous scattering interactions with droplets and other liquid structures in the flow which attenuate and redirect significant portions of the optical signal.

### 1.1 Velocity methods

Single point techniques, such as laser Doppler velocimetry (LDV) and related approaches (Bachalo, 1994), can provide velocity information for specific features of the spray but care must be taken to account for errors in applications where scattering effects cannot be neglected. In general, it is not practical to apply these diagnostics in regions with significant scattering. Moreover, LDV measurements are based on the properties of spherical droplets, and therefore unsuited to the primary atomization regions of high-pressure sprays, where the shape of the liquid structures is often complex.

Laser correlation velocimetry (LCV) is a promising single-point technique which may be applicable to sprays with moderate to high  $OD$  (Chaves et al., 2004). However, interpretation of the LCV information is not straightforward. At present, the technique is suited to monitor spray performance under some conditions, but may be difficult to apply for spray characterization (Hespel et al., 2012).

Particle image velocimetry (PIV) is the preferred technique for velocity imaging, due to the accuracy with which it can be applied, provided that the region of interest can be seeded with tracer particles that follow the flow and provide well-resolved image markers (Raffel et al., 2007). Here, correlation methods are used to extract velocity information from image-pairs or double exposure images dominated by light scattered from the seed particles, allowing the flow to be mapped and tracked.

The prospect of seeding the flow in the present work is undesirable, due to the sensitivity of atomization process. In

addition, much of the velocity data needed to inform our understanding of the spray morphology is concentrated in the shear layers near the liquid/gas interface as well as within the liquid features themselves. These non-laminar, multi-phase conditions, coupled with the large density differential between the liquid and the gas make effective seeding of the flow very difficult. However, the correlation methods applied in PIV can be adapted for calculating velocity from images of unseeded flows (Tokumaru and Dimotakis, 1995).

This approach, generally known as image correlation velocimetry (ICV), uses matching algorithms to calculate velocity either by tagging the flow with trackable features (Krüger and Grünefeld, 1999), matching the motion of naturally occurring features within the flow (Sedarsky et al., 2006), or by predicatively morphing and validating the scalar field (Marks et al., 2010). Here, the form of the measured scalar field and the resulting correlation topology can vary widely compared to the well-behaved intensities generated by seed particles. This difference in the variability and structure of the sampled intensity fields is the fundamental difference between PIV techniques and ICV. The former achieves highly accurate matching by correlating fields with generic, well-separated, and moderately uniform intensity peaks. The latter applies specialized matching approaches to signals which are not structured appropriately or lack the signal-to-noise levels necessary to apply standard PIV analysis.

High-quality results can be obtained with ICV methods, however care must be taken to validate velocity results as the correlation errors associated with unseeded images can be appreciably higher than PIV (Fielding et al., 2001). ICV methods are appropriate for the present work, which requires non-intrusive temporal- and spatially resolved velocity measurements in the near-field regions of a diesel spray.

The objective of this article is to examine the flow conditions of a single-hole diesel fuel injector nozzle. To this end, time-resolved ultrafast shadow images of the fuel spray were acquired at a series of injection pressures and times following the start of injection (SOI). Instantaneous velocities of jet structures and droplets were obtained by matching and validating the motion of liquid-gas boundary features resolved in shadow images of a high-pressure fuel spray.

### 1.2 Resolved feature matching

Although the spray presents the viewer with a complex three-dimensional mass of inhomogeneous features along its centerline, the conical symmetry of plain-orifice jet allows the time-resolved spray periphery to be reliably interpreted as a two-dimensional measurement region (Sedarsky et al., 2012). By positioning the object plane of the imaging system at the center of the spray, the structure and shear layers of the spray edges can be spatially resolved in the limited region bounded by the depth-of-focus of the light collection optics.

In addition, while multiply-scattered light is present in the images, this arrangement emphasizes measurements in the regions of the spray least affected by this noise contribution. The shadow images in this work were generated using a transillumination imaging system, which is discussed in detail in Section 2. Source light for the measurements was supplied by an amplified femtosecond laser system configured for two-pulse operation, with an imaging arrangement similar to the system of Sedarsky et al. (Sedarsky et al., 2009). Here, the light collection and transmission to the image plane result in a depth-of-field of the order of  $150 \mu\text{m}$ , estimated from the optical parameters as discussed in (Sedarsky et al., 2012). However, since the present work is focused on the spray periphery, the optical Kerr effect shutter was omitted in the current implementation.

The details of the image processing and matching procedures used to obtain velocity information are discussed in Section 3, followed by a presentation of statistical velocity profiles compiled from the single-shot velocity results. The velocity profiles given in Section 4 provide a convenient perspective for viewing the relative motion of the jet boundary and ligaments or droplets within the depth-of-field of the imaging system. This approach highlights structural instabilities appearing as the liquid exits the orifice, revealing behavior which influences breakup and the overall morphology of the spray. In Section 5, anomalous behavior of the test injector is identified in the velocity profiles and related to spray morphology visible in individual spray images. Finally, the probable sources of the anomalous breakup modes and spray structure are discussed in light of these velocity results.

## 2 Image acquisition

Sets of time-correlated images were obtained to analyze the kinematics of a diesel fuel injection spray. The spray was illuminated by a double-pulse femtosecond laser system consisting of two synchronized regenerative Ti-Sapphire amplifiers (Coherent Libra) seeded by a common Ti-Sapphire oscillator (Coherent Vitesse, 80 MHz). The short-pulse light from the oscillator is stretched and separated into two beams, which are amplified as they traverse the gain medium in their respective amplifiers. After compression, the two beam paths are recombined to form a single beam containing pairs of pulses with precisely known time separations.

By adjusting the selection of oscillator pulses entering the amplifiers, the delay between consecutive output pulses can be adjusted from  $12.5 \pm 2 \text{ ns}$  to  $500 \mu\text{s}$ . Here, the adjustment step corresponds to the period of the oscillator, and the variability in the adjustment stems from the possible optical path differences between selected oscillator pulses.

The resulting source light is a 1 kHz train of 100 fs pulse-pairs, confined to a low divergence beam with a 10 mm di-

ameter, a center wavelength of 800 nm, and an average energy per pulse of 3.7 mJ. The oscillator, amplifiers and beam combination optics are carefully adjusted to obtain similar pulses in each pair, in terms of pulse duration, amplitude, optical alignment, and polarization.

This two pulse beam was directed toward the injector which is housed in a vented (atmospheric pressure) enclosure with optical access to facilitate the study of relevant fuels without contaminating the system optics. The measurements were carried out using a calibration liquid (Shell NormaFluid, ISO 4113) with properties similar to diesel fuel and precisely controlled viscosity, density, and surface tension specifications (see Table 1).

**Table 1** Properties of ISO 4113 calibration oil.

Density	Viscosity	Surface Tension
$821 \text{ kg/m}^3$	$0.0032 \text{ kg/(m}\cdot\text{s)}$	$0.02547 \text{ N/m}$

The injector nozzle used in the measurements was a hydro-ground, plain-orifice test nozzle with a conical micro-sac construction and needle valve closure. The injector was designed to produce a single-hole spray related to fuel delivery from a 6-hole commercial diesel fuel injector. A schematic view of the nozzle is given in Fig. 1, together with a view of the specific internal geometry given at 4 different angles by x-ray transmission shadowgrams. The relevant nozzle and spray parameters are listed in Table 2.

**Table 2** Test nozzle and injection parameters.

Nozzle properties	Spray conditions
$P_{inj} = 40\text{--}100 \text{ MPa}$	$P_{back} = 0.1 \text{ MPa}$
$C_d = 0.84$	$U_B = 300\text{--}500 \text{ m/s}$
$K_N = 1.002$	$Re = 9000\text{--}14000$
$\ell/d = 5.66$	$We = 1140\text{--}1800$

The injector assembly was mounted on three-way translation stage, and fuel was delivered to the injector housing by a pump through a Common-Rail accumulator capable of supplying system pressures up to  $\sim 100 \text{ MPa}$ . The start and duration of each injection event was set by the action of a balanced servo solenoid mechanism which allows precise control of needle lift. Each injection event was driven electronically by a staccato-style current pulse of  $400 \mu\text{s}$  duration, delivered to the injector at a repetition rate of 1 Hz, where the reference clock for the complete system was sourced from the laser oscillator (80 MHz). In this arrangement the onset of each injection event was subject to timing jitter on the order of  $1 \mu\text{s}$ , creating a sizeable systematic error with regard to precise measurement timing relative to SOI. This

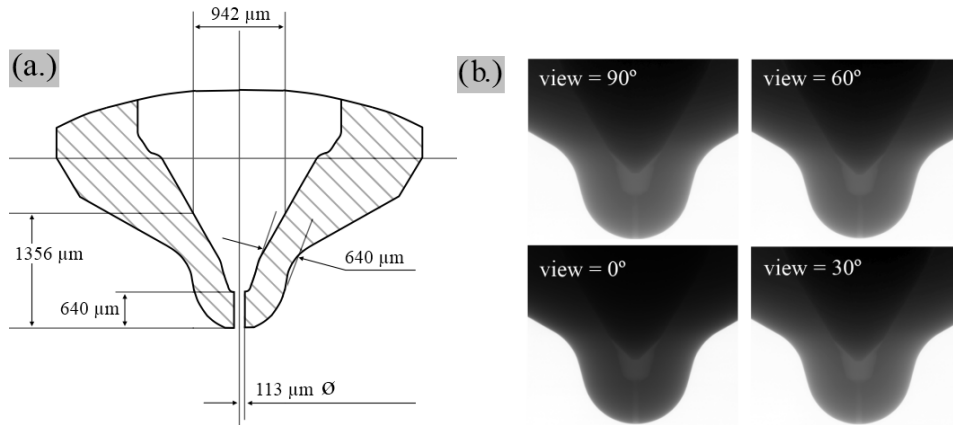


**Fig. 1** Detailed views of the diesel test injector nozzle: (a) Schematic view; (b) X-ray transmission shadowgrams showing internal geometry at 0, 30, 60, and 90°.

uncertainty was reduced by noting that jet penetration length for a high pressure diesel spray is a linear function of time at early injection times (see Fig. 2). For each separate time

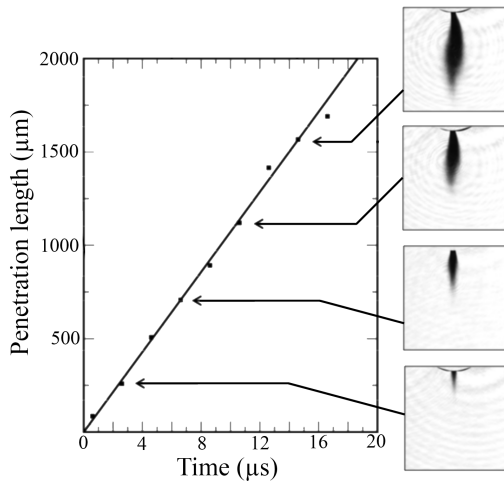


**Fig. 2** Average jet penetration vs. time. The inset images show the liquid jet, averaged over 200 shots. Precise injection timing from SOI in each measurement was identified by penetration level, which is a linear function of time for early injection times.

delay case, the hydrodynamic starting time of the injection was extrapolated from the average jet penetration length, determined from sets of 200 images. The shadow images formed by source light interaction with the spray were subsequently imaged to an interframe transfer CCD array (PCO integrated by LaVision), at approximately 7:1 magnification. Each frame was exposed to light from a single source laser pulse such that the 100 fs duration of each pulse ensured the motion of the jet and laboratory seeing conditions were effectively frozen in each image. The minimum time interval between the first and second frame in the image pair was limited to  $\sim 150$  ns by the frame transfer time of the CCD.

The resolution of the complete imaging system was on the order of  $7 \mu\text{m}$ .

Using this experimental setup, pairs of images with precisely controlled time separations were recorded. Figure 3 shows an example image for an injection pressure of 60 MPa. Here, the fuel jet can be seen issuing from the tip of the injector located at the top of the frame and the diameter of the injector orifice ( $113 \mu\text{m}$ ) indicates the spatial scale. Distinct liquid fragments and the edges of the jet which coincide with the object plane appear sharply focused in the image. Structure and droplets near the depth-of-field limits are also apparent but exhibit lower contrast and small amounts of distortion consistent with defocusing. The signature of this distortion allows out-of-focus regions to be excluded from the velocity analysis (Sedarsky et al., 2012). Likewise, the large diffraction rings faintly visible in the background of Fig. 3 have negligible influence on velocity results, since the focused features present higher signal levels which dominate the correlation response.

### 3 Velocity computation by image processing

The calculations and data analysis discussed in the following section were implemented in an in-house image analysis code based on OpenCV (Bradski and Kaehler, 2008) and developed for detailed examination of spray kinematics and fluid motion. By identifying persistent spatial intensity variations which are present in consecutive images, the velocity of time-resolved liquid structures in spray images can be estimated. This approach allows distinctive features in one image to be exploited by correlation methods to track changes in one or more subsequent images which are directly related to structure motion and the kinematics of the spray.

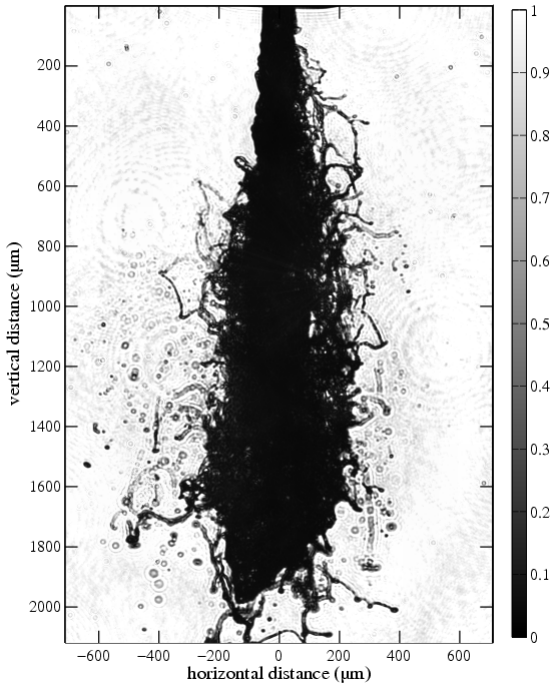


**Fig. 3** Shadow image of a diesel jet issuing from a 113  $\mu\text{m}$  plain orifice test injector into ambient air, 18  $\mu\text{s}$  after SOI;  $P_{inj} = 60$  MPa.

### 3.1 Correlation approach

On a basic level, the image data present a discretely sampled spatial intensity pattern which indicates the underlying fluid structure. By considering the amplitude and texture of the pattern within separately chosen spatial extents (templates), localized feature sets can be formed from intensity data taken at time,  $t_1$ . These templates are matched to the patterns within subregions (search fields) chosen from subsequent intensity data taken at time,  $t_2 = t_1 + \Delta t$ , yielding new spatial coordinates. Assuming constant local image intensity, the displacement given by the coordinate shift for each template/search pair indicates fluid motion over the time interval,  $\Delta t$ . Figure 4 shows an example of one such set of image subregions, together with the indicated match result.

Each template region is matched within its corresponding search field by identifying the peak of the normalized cross correlation, given by:

$$\frac{1}{n-1} \sum_{x,y} \frac{1}{\sigma_S \sigma_T} (S(x,y) - \bar{S})(T(x,y) - \bar{T}) \quad (1)$$

where  $x$  and  $y$  represent horizontal and vertical image coordinates.  $T(x,y)$  is the template region,  $S(x,y)$  is the search field,  $n$  is the sum of the samples (pixels) from the search and template regions,  $\sigma_S$  and  $\sigma_T$  represent the standard deviation of  $S(x,y)$  and  $T(x,y)$ , and  $\bar{T}$  and  $\bar{S}$  represent the respective average intensities of the template and search regions.

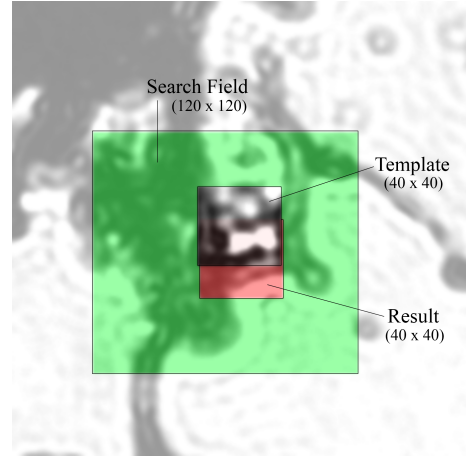


**Fig. 4** Image subregions for correlation matching analysis. Each vector, as shown in Fig. 5, represents the displacement of a sample region (Template) to its best equivalent match (Result) within the Search Field region.

Thus, the general procedure for obtaining accurate velocity vectors from the raw image data consists in: preparing image data, selecting template locations, choosing search and template region sizes, and finally matching and validating correlation results.

### 3.2 Data preparation and sampling

To minimize the relative error in the structure motion calculation, the inter-frame time separation,  $\Delta t$ , was set to allow substantial displacement of tracking features with negligible distortion in the intensity structure. A time delay on the order of 260 ns was found to work well for following spray motion generated by the current system (see Table 2).

The correlation method given by Eqn. 1 implicitly requires that the tracked features are minimally distorted between measurements, and undergo translation, with negligible rotation, expansion, contraction, and occlusion. This sets an upper limit on the acceptable time-delay for cross-correlation of independent spatial intensity measurements. A lower limit of the acceptable time-delay is imposed by the spatial resolution and sensitivity of the imaging system, as smaller motions increase detection requirements along with relative measurement uncertainty. In the present case, however, the minimum time-delay for the system is limited well above this level by the frame-transfer timing of the detector.

Raw image data is adjusted prior to correlation analysis to ensure that the data is consistent with the assumptions necessary to interpret pattern movement as displacement of the imaged structure. Specifically, we require the image-pairs to be registered to the same coordinate space, have a constant local intensity (flat field), and minimal distortion ( $\Delta t$  is small relative to the detected velocity).

Since the matching approach discussed here is sensitive to intensity fluctuations over the image, variations which are unrelated to the measured structure should be minimized to avoid influencing the matching process. In order to account for non-uniform illumination and sensor effects, the data collected for each image includes dark and ‘no signal’ frames generated under the same conditions. This extra data is used to apply a flat-field intensity correction to each image (Newberry, 1991). All images are generated using the same source and detector, so image-pairs are spatially synchronized without the need for image registration or adjustments.

The cross-correlation of patterns formed by distributed structures with limited variability can yield correlation coefficient topology with no clear maxima, leading to displacement results which do not reflect the motion of the underlying structure. This problem was addressed by identifying image regions with significant variation and preferentially selecting these regions to form the templates for correlation analysis. Target pixels used to locate the centers of template regions were selected by thresholding the normalized image data and applying Canny edge detection (Luo and Duraiswami, 2008) to identify image coordinates near strong intensity gradients.

### 3.3 Window sizing

Accurate matching results depend on the identification of trackable image regions and the selection of correlation window sizes which are suited to both the spatial scale of the matched features and the time-separation of the image data to be correlated. In most cases, effective template regions should be large enough to loosely frame smaller structures of interest, with corresponding search field regions 2 to 3 times the template dimensions. It is worthwhile to note that normalized cross-correlation is computationally expensive (scaling as  $O(n * \log n)$ ) and smaller functional window sizes are preferable. In addition, the combination of template and search field sizes naturally limit the range of detectable motion for the cross-correlation application. In the limit of small templates, matching entropy is low, possibly resulting in errors from ambiguous feature matching. In the limit of small search field size, maximum displacement is severely constrained. For large templates, displacement is likewise heavily constrained. Large template regions can also limit the spatial resolution of the estimated velocity.

The optimal template and search field sizes depend on the size, form, and intensity signature of the features of interest as well as the motion of the underlying structure and time-separation of the image data. Window sizes which are well-suited to the underlying data increase the efficiency of feature identification and reduce the likelihood of erroneous pattern matching.

### 3.4 Vector validation procedures

The cross-correlation operation for each template yields a match result and displaced spatial coordinates which, together with the initial template coordinates, represent a velocity for the identified feature set. With properly sized correlation regions and significant variation in the template pattern, this match result should indicate the motion of the underlying fluid structure. However, a number of circumstances can result in matches which are known to be, or likely to be false, such as edge cases, poorly structured templates, or low coefficient matches.

To identify and exclude these vectors, the velocity data and their associated image sub-regions are validated against a list of criteria which examine the spatial variance and texture energy of the image regions, as well as the correlation strength and boundary constraints of the matching results. The validation procedures fall roughly into two categories: threshold, or ‘relative constraint’ criteria, and absolute criteria. The threshold criteria are user-selectable limits which can be set to eliminate weakly matching patterns which are likely to yield erroneous vectors. Absolute criteria are pass/fail tests, such as boundary constraints which eliminate vectors indiscriminately. The settings for effective validation do not vary widely, but as with correlation window sizing, the optimum settings depend on the feature sets, interframe delay, and underlying motion in the images. The combination of the targeted selection of template regions and the threshold validation criteria effectively limit the velocity results to in-focus edge features of the spray (Sedarsky et al., 2012). Figure 5 shows displacement vectors calculated from one image-pair near the leading edge of the spray shown in Fig. 3.

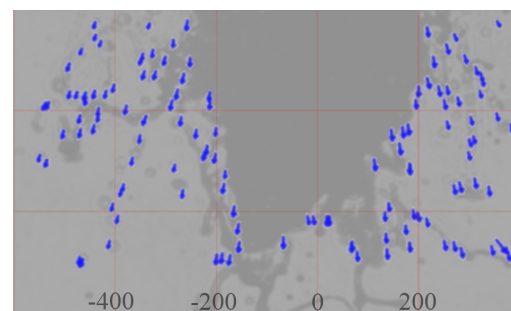


**Fig. 5** Velocity vectors of the leading edge of the spray shown in Fig. 3, with corresponding  $\mu\text{m}$ -scale spatial grid.

It is important to point out that the results discussed here represent (2D) planar motion of observed liquid structures—the projection of the real structure (3D) velocity in the object plane of the imaging system. Given the geometry of the plain-orifice jet, one can postulate that the third (unknown) component of the velocity is on the order of the measured

horizontal velocity component. In addition, it may be possible for the velocity of the observed structures to differ from the velocity of the liquid itself, in which case the quantitative application of these measurements would be limited. Nevertheless, the kinematics presented here can be readily applied for comparative evaluation of high pressure injection conditions, and accurate relative statistics on velocity can still be useful, especially for the validation of numerical simulations.

#### 4 Statistical description of the injector

A statistical evaluation of the diesel test injector was conducted by compiling the instantaneous velocities calculated from pairs of time-resolved images to form data sets, fixed at different times relative to SOI. Sets composed of 200 image-pairs were recorded and processed to obtain instantaneous velocity fields. The vectors corresponding to these image results (2048x2048) were subsequently partitioned into 20x20 pixel cells. In each of these square bins, the magnitudes of the computed vectors originating from the region were averaged to yield a mean velocity magnitude assigned to the cell. The grid size was chosen to provide a reasonable compromise between sample statistics and coarseness of the sample groups. In addition, the 20x20 cell size was small enough to permit permutation and averaging of the grid placement allowing sub-grid resolution profiles, further increasing the accuracy of the results.

The statistical relevance of the mean velocity for each region is directly related to the number of vectors contributing to the block. On this basis, cells containing less than 20 vectors were excluded from the analysis to improve the significance of the computed results. The velocity profiles derived from the data sets were arranged to form a time-ordered series which was then used to chart spray behavior over the course of the fuel injection event.

The targeting and validation procedures mentioned in section 3 ensure that out-of-focus elements of the image-pairs do not contribute significantly to the velocity calculations. As a consequence, the statistical velocity profiles exhibit a central region devoid of vectors which corresponds roughly to the average jet position for each time-delay.

Figures 7, 8, and 9 show the mean velocity as a function of the location for different delays from the start of injection. Examining figure 7, at very early time-delays we observe the expected velocity profile, with the early jet extending centrally and slightly slower velocities distributed on the portions of the jet with more lateral motion. For the first 10  $\mu\text{s}$  after SOI, the flow is reasonably symmetric, and the velocity profile initially appears uniformly distributed about the nozzle orifice. Figure 7 shows this uniform behavior with only small speed differences visible between the left (fast) and right (slow) sides of the spray at 15  $\mu\text{s}$  after SOI.

As the spray becomes more established, however, a disparity in the velocity profile becomes apparent, as evidenced by the progression from 20 to 35  $\mu\text{s}$  shown in Fig. 8. The evolution of the spray continues with the fast and slow sides of the jet becoming more pronounced, reaching differentials of 90 m/s by 40  $\mu\text{s}$ . This asymmetric profile continues to intensify as the spray develops. Increasing speeds can be observed on the slow side of the jet profile as well, as the jet expands downstream. Nevertheless, strong differences in velocity across the jet profile are apparent through the entire range as the flow evolves, before reaching a steady flow condition at around 55  $\mu\text{s}$  after SOI.

In order to understand the shape of the liquid jet, the injector was rotated around the vertical axis and sets of 200 image-pairs were acquired at 6 different angles for additional velocity analysis. Figure 6 shows a map of the velocity field from liquid structure motion for angles of 0°, 26°, 66°, 96°, 126° and 156° chosen from an arbitrary reference. These data were calculated from the fully developed spray, for a time-delay  $\sim 55 \mu\text{s}$  after SOI. These measurements confirm that the present injector produces an asymmetric velocity profile, which may be a consequence of cavitation and irregular flow inside the injector. Note that this behavior is persistent and reproducible; the distinct fast and slow sides of the injector remain the same for every injection event.

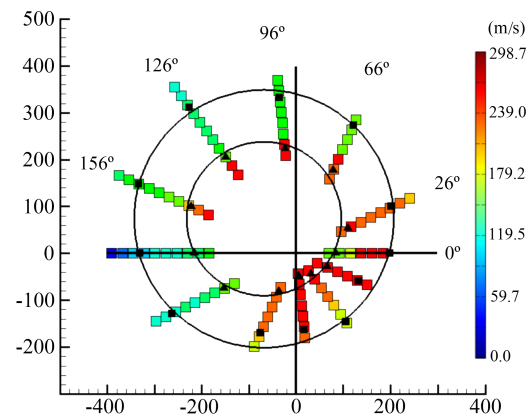


**Fig. 6** Top-down view of velocity profiles for single-hole diesel test nozzle, showing results compiled from image data and velocity analysis of the spray at a range of angles. The spatial scale is given in  $\mu\text{m}$ , and the colorbar represents velocity magnitude in units of m/s. The inner and outer circles are fit to the edges of the jet 1 mm downstream from the nozzle orifice. The edges are calculated from spray images averaged over 200 shots and detected at the 20% and 80% threshold levels to show the variability and extent of the spray.

In order to reconstruct the shape of a section of the spray, the diameter of the jet at a position 1 mm downstream from the nozzle orifice is plotted for different nozzle viewing angles in Fig. 6. The inner and outer circles shown in Fig. 6

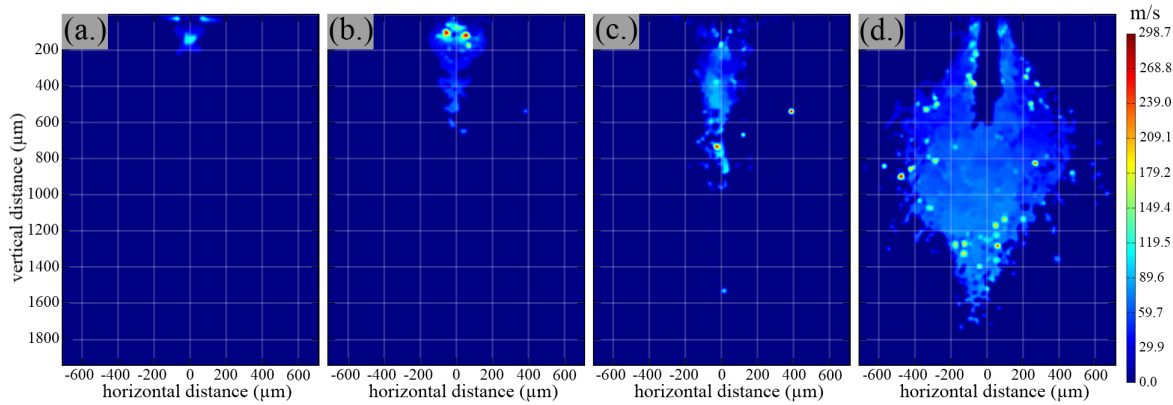


**Fig. 7** Velocity profiles of the diesel test injector (see table 2), shown for a series of time-delays after SOI: (a)  $2 \mu\text{s}$ . (b)  $5 \mu\text{s}$ . (c)  $10 \mu\text{s}$ . (d)  $15 \mu\text{s}$ .  $P_{inj} = 60 \text{ MPa}$ ;  $Re = 11 \text{ k}$ ;  $We = 1400$ .

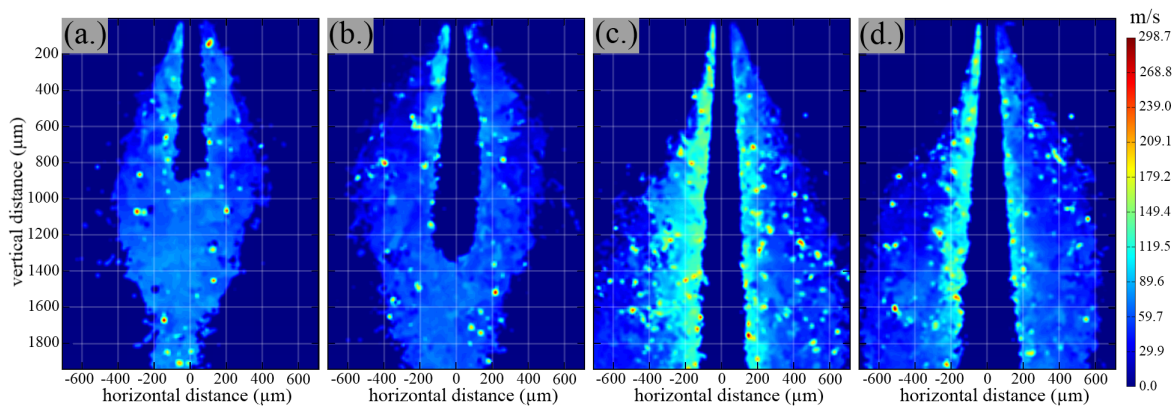


**Fig. 8** Velocity profiles of the diesel test injector (see table 2), shown for a series of time-delays after SOI: (a)  $20 \mu\text{s}$ . (b)  $25 \mu\text{s}$ . (c)  $30 \mu\text{s}$ . (d)  $35 \mu\text{s}$ .  $P_{inj} = 60 \text{ MPa}$ ;  $Re = 11 \text{ k}$ ;  $We = 1400$ .

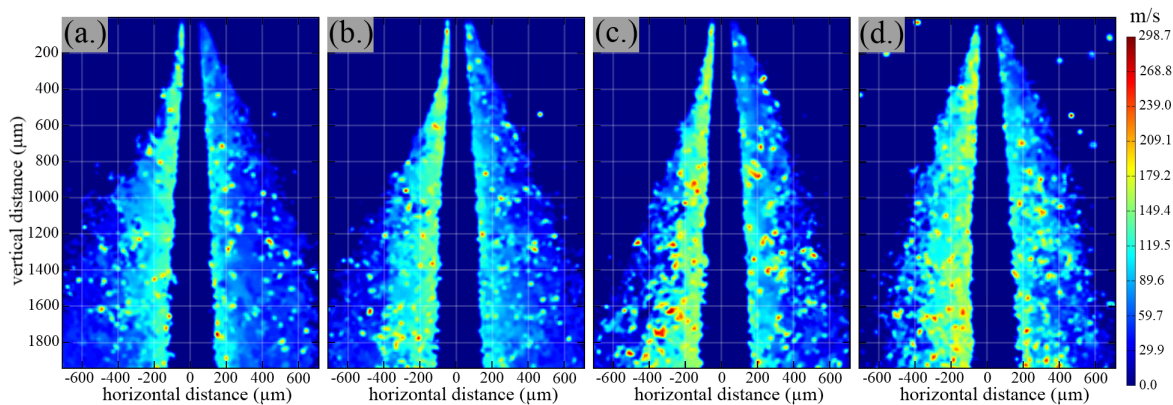


**Fig. 9** Velocity profiles of the diesel test injector (see table 2), shown for a series of time-delays after SOI: (a)  $40 \mu\text{s}$ . (b)  $45 \mu\text{s}$ . (c)  $50 \mu\text{s}$ . (d)  $55 \mu\text{s}$ .  $P_{inj} = 60 \text{ MPa}$ ;  $Re = 11 \text{ k}$ ;  $We = 1400$ .

delineate the average periphery of the spray derived from 200 images for each angle.

Given the shot-to-shot variability in the form and motion of the jet, the calculated location of the outer edge of the spray is sensitive to the choice of gray-level threshold used in the edge-finding algorithm. To show the range of this variability, two levels are shown in the figure, where the

inner and outer lines are fit to data calculated with 20% and the 80% threshold levels, respectively. These lines show approximately circular cross-sections, with centers which are shifted from the center of the nozzle orifice in the direction of the low-velocity side of the spray.

The colored lines radiating from the orifice position and indicated by the angle labels in Fig. 6 show the velocity

magnitude profile for each rotation angle. The distribution of velocity in the profiles clearly indicates distinct fast and slow sides of the spray, approximately centered at  $126^\circ$ . The velocity differences apparent in this angular view are consistent with the deflection of the liquid jet which is visible in the spray images. This deflection angle was estimated from the spray periphery data to be  $\sim 5.5^\circ$ .

The lack of symmetry between the velocity profiles for each angle implies that the out-of-plane component may be significant for angles which are not aligned to the side of the jet, i.e. direct views of the fast or slow sides of the jet, such as the profile for  $26^\circ$  shown in Fig. 6. This is important for effective use of the velocimetry approach applied in this work, which measures velocity confined to the object plane of the imaging setup and is unable to determine the out-of-plane component of the structure motion.

## 5 Atomization behavior

The large velocity differences observed in the liquid structures on opposing sides of the jet accompany changes in the prevailing atomization conditions across the spray. Figure 10 shows example images of the fully developed spray viewed from the  $126^\circ$  position, as shown in Fig. 6. Here, the left-hand edge (fast side) of the jet exhibits the highest average liquid structure velocities while the right-hand edge (slow side) directly opposite exhibits the lowest average velocities.

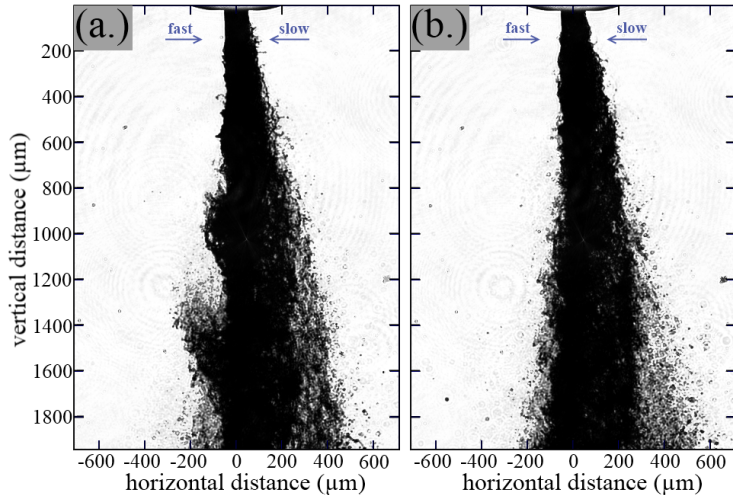


**Fig. 10** Example images showing the  $126^\circ$  view (see Fig. 6) of the test injector spray. Two different atomization processes are apparent on the left side of the liquid column, which corresponds to the highest liquid velocity.  $55\mu\text{s}$  after SOI;  $P_{inj} = 60\text{ MPa}$ .

As noted above, the trajectory of the liquid column exhibits an angular deflection in the direction of the slow side of the nozzle outlet. This deflection extends the slow edge

laterally as the spray is established, increasing the exposed shear surface and perturbing boundary layers forming at the spray edge. These are small effects under the current conditions, but they contribute to the asymmetric form of the flow and the spread of the droplets distributed on the slow side of the jet, as seen on the right side of both images shown Fig. 10.

The slow side of the jet begins to breakup in the vicinity of the nozzle within 1 or 2 nozzle diameters. The jet surface near the orifice is rough as it exits, including small disturbances which contribute to momentum exchange, entrainment with the surrounding air, and shearing of liquid from the jet surface.

The character of the atomization on the fast side of the jet differs significantly from the slow side kinematics. At first, the trajectory of the liquid along the edge curves inward and on average, droplets are dispersed at a greater distance from the nozzle. The jet surface near the orifice appears undisturbed and a smooth liquid column extends, in most cases, for 2 to 5 nozzle diameters before air entrainment and shear effects begin to disturb the jet.

Distinct macrostructure appears on the fast side of the spray under the asymmetric velocity conditions. In about half the cases, the breakup on the fast side of the spray resembles the slow edge, with shear forces driving Kelvin–Helmholtz instabilities which grow to form ligaments and small droplets. However, breakup on the slow edge happens more rapidly, with droplets and structure appearing earlier and with more intricate interaction. In other cases, small instabilities become apparent on the fast side within the first few nozzle diameters and quickly grow to produce large waves which periodically shed larger droplets and ligaments. This behavior is intermittent and present throughout the range of injection pressures available with the current system. Figure 10 includes two example images from the same data set which show both of these breakup modes for the same view angle and identical conditions.

Reproducible asymmetric needle motion has been observed in diesel fuel injectors and shown to contribute to flow irregularities (?). However, the flow velocity differences and transient atomization modes with periodic structure observed here resemble flow structures which are often seen in the presence of cavitation produced under controlled conditions in scaled, transparent test nozzles. This likeness suggests that the observed flow conditions are the result of cavitation and fluctuating pressure conditions in the fluid upstream of the nozzle orifice.

Studies of cavitating flows show that viscous stress and pressure effects largely determine the inception of cavitation within the channel upstream of the orifice (Dabiri et al., 2007, 2010). Here, vortices formed near the inlet can lead to local pressure and temperature conditions which induce the production of vapor from the bulk liquid. The formation and

subsequent collapse of bubbles in the fluid give rise to pressure waves which can interact to form oscillatory behavior and instabilities which are apparent in the emerging spray (Mauger, 2012). Figure 11 shows measurements and simulation results from previous work (Giannadakis et al., 2008) comparing a single-hole injector flow with sharply edged (top) and hydroground nozzles (bottom) for flow conditions comparable to test injector presented in this work.

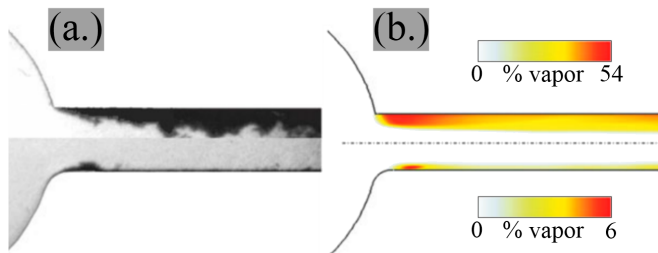


**Fig. 11** Half-nozzle diesel injection ( $P_{inj} = 50$  MPa,  $Re \approx 19k$ ) images and simulations for sharply edged (top) and hydroground nozzles (bottom). Part (a) shows time-resolved shadowgrams of cavitation vapor from König & Blessing (2000). Part (b) shows simulation results of mean cavitation vapor distribution (volume percentage) from Giannadakis, et al. (2008).

The shadowgrams of the nozzle interior shown in figure 11(a) give a qualitative view of the formation and propagation of cavitation in the channel. Figure 11(b) shows the amount and spatial extent of cavitation vapor predicted by the simulations of Giannadakis for these flow conditions.

Note that the nozzle used in the present work is operated at a lower Reynolds number than the flows presented in Fig. 11, and the nozzle construction corresponds to the cases shown in the bottom half of figs. 11(a) and 11(b). Consequently, modest amounts of cavitation and a symmetric general profile are expected in the flow according to the test injector design. Nevertheless, strong differences are apparent between fast side and slow sides of the spray, and intermittent changes in the morphology of the spray under identical conditions indicate that transient phenomena are active in the formation of the spray.

X-ray microscopy images of the injector with  $\sim 20 \mu m$  resolution (see Fig. 1) were taken for a range of angles about the central axis. These images indicate a symmetric nozzle construction with no visible irregularities. However, it is possible that a material defect or error in the machining process has left an uneven region at the channel inlet which was not covered by the microscopic inspection. Gross differences in velocity and deflection have been observed in single-hole sprays in some conditions when a portion of the inlet lip is lower (exhibiting a different curvature) than the surrounding edge. This can lead to vortex interactions which encourage midstream or string cavitation along one side of

the channel, reducing the effective area of the orifice and creating asymmetric flow conditions (Danckert and Affolter, 2001).

The onset of the velocity disparity across the injector is consistent with a cavitation or dynamic pressure condition, where small pockets of vapor form as a critical velocity is reached some time  $\sim 10 \mu s$  after SOI. Pockets of gas forming in the flow could then serve to isolate the liquid from the wall of the channel, disturbing the boundary layer and giving rise to turbulence in the internal flow. This in turn would promote small scale instabilities which contribute to the prevalence of different atomization conditions on each side of the spray.

Even when vortex effects do not produce cavitation directly, pressure fluctuations set up in the channel as a result of the interaction can contribute to spray instabilities and periodic behavior appearing in the downstream regions of the flow. It is likely that the large oscillatory features appearing on the fast edge of the diesel spray are the result of pressure fluctuation dynamics related to cavitation which grow to destabilize the liquid column as they propagate downstream.

## 6 Conclusions

A statistical description of a single-hole diesel fuel injection spray, including high-resolution velocity information, was compiled from ultrafast imaging measurements.

The time-resolved spray measurements were made with an imaging system synchronized to a dual-pulse femtosecond laser source, allowing the acquisition of time-correlated image-pairs which are spatially resolved by the optics. Correlation analysis was successfully applied to these image results to calculate the instantaneous spray velocity related to the time-step for each image-pair.

This approach is able to effectively map the early time-evolution of the spray. In the case of the current injector, it reveals large disparities in the liquid structure velocity in different regions across the spray.

Given the flow conditions and the construction of the nozzle studied here, it is likely that the transient atomization behavior and asymmetric flow conditions exhibited by the test injector are the result of an irregularity in the nozzle inlet, causing cavitation and asymmetric pressure fluctuations within the nozzle itself. This conclusion is consistent with the form of the observed breakup modes, the deflection of the fuel jet, and would explain the asymmetric velocity behavior measured by the ultrafast ICV statistics.

Statistically significant collections of spray data compiled from these spatial- and temporally resolved single-shot measurements provide an effective and relatively straightforward view of spray structure velocities which are relevant to primary breakup and atomization in multiphase flows.

**Acknowledgements** This work was supported by NADIA-Bio program, with funding from the French Government and the Haute-Normandie region, in the framework of the Moveo cluster (“private cars and public transport for man and his environment”).

## References

- W. D. Bachalo. Experimental methods in multiphase flows. *International Journal of Multiphase Flow*, 20(0):261 – 295, 1994.
- G. Bradski and A. Kaehler. *Learning OpenCV: computer vision with the OpenCV library*. O’Reilly Media, 1 edition, Sept. 2008. ISBN 978-0-596-51613-0.
- H. Chaves, C. Kirmse, and F. Obermeier. Velocity measurements of dense diesel fuel sprays in dense air. *Atomization and Sprays*, 14(6), 2004.
- S. Dabiri, W. A. Sirignano, and D. D. Joseph. Cavitation in an orifice flow. *Physics of Fluids*, 19(7):072112.1–072112.9, 2007.
- S. Dabiri, W. A. Sirignano, and D. D. Joseph. A numerical study on the effects of cavitation on orifice flow. *Physics of Fluids*, 22(4):042102–042102–13, 2010.
- B. Danckert and P. K. Affolter. Ways of nozzle geometry optimisation for new injection systems, fulfilling future emission limits. In *Proc. of the 23rd World Congress on Combustion Engine Technology for Ship Propulsion, Power Generation, Rail Traction*, volume 2 of *Proceedings of CIMAC*. CIMAC, May 2001.
- J. Fielding, M. B. Long, G. Fielding, and M. Komiyama. Systematic errors in optical-flow velocimetry for turbulent flows and flames. *Applied Optics*, 40(6):757–764, Feb. 2001.
- E. Giannadakis, M. Gavaises, and C. Arcoumanis. Modelling of cavitation in diesel injector nozzles. *Journal of Fluid Mechanics*, 616:153–193, 2008.
- C. Hespel, J.-B. Blaisot, M. Gazon, and G. Godard. Laser correlation velocimetry performance in diesel applications: spatial selectivity and velocity sensitivity. *Experiments in Fluids*, 53(1):245–264, July 2012.
- S. Idlahcen, C. Rozé, T. Girasole, and J.-B. Blaisot. Sub-picosecond ballistic imaging of a liquid jet. *Experiments in Fluids*, 52(2):289–298, 2012.
- E. Kristensson, M. Richter, and M. Aldén. Nanosecond structured laser illumination planar imaging for single-shot imaging of dense sprays. *Atomization and Sprays*, 20(4):337–343, Sept. 2010.
- S. Krüger and G. Grünefeld. Stereoscopic flow-tagging velocimetry. *Applied Physics B: Lasers and Optics*, 69(5): 509–512, 1999.
- R. Lebas, T. Ménard, P. A. Beau, A. Berlemont, and F. X. Demoulin. Numerical simulation of primary break-up and atomization: Dns and modelling study. *International Journal of Multiphase Flow*, 35(3):247 – 260, 2009.
- M. A. Linne, M. E. Paciaroni, E. Berrocal, and D. Sedarsky. Ballistic imaging of liquid breakup processes in dense sprays. *Proc. of the Combustion Institute*, 32:2147–2161, 2009.
- Y. Luo and R. Duraiswami. Canny edge detection on nvidia cuda. In *Computer Society Conference on Computer Vision and Pattern Recognition Workshops*, Proceedings of CVPRW, pages 1–8. IEEE, june 2008.
- T. K. Marks, J. R. Hershey, and J. R. Movellan. Tracking motion, deformation, and texture using conditionally gaussian processes. *Pattern Analysis and Machine Intelligence, IEEE Transactions on*, 32(2):348 –363, feb. 2010.
- C. Mauger. *Cavitation dans un micro-canal modèle d’injecteur diesel : méthodes de visualisation et influence de l’état de surface*. PhD thesis, University of Lyon, Apr. 2012.
- T. Ménard, S. Tanguy, and A. Berlemont. Coupling level set/vof/ghost fluid methods: Validation and application to 3d simulation of the primary break-up of a liquid jet. *International Journal of Multiphase Flow*, 33(5):510 – 524, 2007.
- M. V. Newberry. Signal-to-noise considerations for sky-subtracted ccd data. *Publications of the Astronomical Society of the Pacific*, 103(659):122–130, 1991.
- M. Raffel, C. E. Willert, S. T. Wereley, and J. Kompenhans. *Particle image velocimetry : a practical guide*. Springer, New York, 2 edition, 2007. ISBN 9783540723073.
- A. Ramírez, S. Som, S. Aggarwal, A. Kastengren, E. El-Hannouny, D. Longman, and C. Powell. Quantitative x-ray measurements of high-pressure fuel sprays from a production heavy duty diesel injector. *Experiments in Fluids*, 47(1):119–134, 2009.
- D. Sedarsky, M. E. Paciaroni, M. A. Linne, J. R. Gord, and T. R. Meyer. Velocity imaging for the liquid-gas interface in the near field of an atomizing spray: proof of concept. *Opt. Lett.*, 31(7):906–8, 2006.
- D. Sedarsky, J. R. Gord, C. Carter, T. R. Meyer, and M. A. Linne. Fast-framing ballistic imaging of velocity in an aerated spray. *Opt. Lett.*, 34(18):2748–2750, 2009.
- D. Sedarsky, E. Berrocal, and M. A. Linne. Quantitative image contrast enhancement in time-gated transillumination of scattering media. *Opt. Express*, 19(3):1866–1883, Jan 2011.
- D. Sedarsky, S. Idlahcen, J.-B. Blaisot, and C. Rozé. Planar velocity analysis of diesel spray shadow images. In *Proc. of multiphase flow and transport phenomena*, MFTP, Apr. 2012.
- U. Shavit and N. Chigier. Fractal dimensions of liquid jet interface under breakup. *Atomization and Sprays*, 5(6): 525–543, 1995.
- P. T. Tokumaru and P. E. Dimotakis. Image correlation velocimetry. *Experiments in Fluids*, 19:1–15, 1995.